# Dynamics of strong-field laser-induced microplasma formation in noble gases

D. A. Romanov,[1,2] R. Compton,[1,3] A. Filin,[1,3] and R. J. Levis[1,3]

[1]*Center for Advanced Photonics Research, College of Science and Technology, Temple University, Philadelphia, Pennsylvania 19122, USA*

[2]*Department of Physics, Temple University, Philadelphia, Pennsylvania 19122, USA*

[3]*Department of Chemistry, Temple University, Philadelphia, Pennsylvania 19122, USA*

(Received 11 November 2009; published 4 March 2010)

The ultrafast dynamics of microplasmas generated by femtosecond laser pulses in noble gases has been investigated using four-wave mixing (FWM). The time dependence of the FWM signal is observed to reach higher intensity levels faster for Xe, with progressively lower scattering intensity and longer time dynamics for the noble gas series Xe, Kr, Ar, Ne, and He. The temporal dynamics is interpreted in terms of a tunnel ionization and impact cooling mechanism. A formalism to interpret the observed phenomena is presented here with comparison to the measured laser intensity and gas pressure trends.

DOI: 10.1103/PhysRevA.81.033403 PACS number(s): 32.80.Rm, 42.65.Dr, 52.25.Os

## I. INTRODUCTION

The interaction of intense, ultrafast lasers with noble gases has resulted in the discovery of methods to produce high-harmonics [1,2] attosecond pulses [3–5], terahertz generation [6–8], filamentation [9,10], and self-phase modulation used to produce high-bandwidth pulses [11]. Understanding each of these processes involves the excitation, ionization, and propagation of electrons in the intense laser field. For example, the dynamics of high-harmonic generation have been modeled using a few simple parameters [12] to capture the tunnel ionization, subsequent propagation of the electron in the laser field, and recombination with the ion to produce the high-harmonic radiation.

In the laser-induced microplasma process, the electron concentration and temperature dynamics continue to evolve long after the initial excitation or ionization has occurred. A considerable amount of research has focused on determining the electron concentration in femtosecond laser-induced plasmas including interferometry [13,14], longitudinal diffractometry [15], in-line holographic imaging [16–18], electric conductivity [19,20], and shadowgraphic techniques. Shadowgraphic measurements are performed by measuring either the absorption of a probe laser as a consequence of inverse Bremsstrahlung [21] or the change in the refractive index gradient on a probe [22]. Combined shadowgraphic and interferometric imaging [23] has been employed to determine electron collision and recombination time, in addition to the electron density. A direct comparison between the shadowgraphic and interferometric techniques [24] revealed that the shadowgraphic method provided the highest spatial resolution for microplasma formation in air with a 150-fs pulse. The aforementioned techniques reveal electron densities ranging from $\sim 10^{15}$ to $\sim 10^{19}$ $e^-$ cm$^{-3}$. However, the density and diameter of plasmas formed within laser-induced filaments exhibit a complicated dependence on external focusing conditions [25]. In addition, other experimental conditions such as pulse duration and filamentation medium (air, silica, etc.) make direct comparison of electron density measurements difficult. The effects associated with multiple filamentation [26] were often not considered.

The Stark-broadening of emission lines provides an additional means to measure electron density [27,28], and this method has recently been used to compare the electron dynamics for femtosecond and nanosecond laser-induced plasmas [29,30]. Spectroscopic analysis has also been employed to measure the electron temperature dynamics in plasmas generated with femtosecond-duration pulses [29,30]. Several methods have been used, including the Boltzmann relation and the relative line-to-continuum intensity ratio [31,32], both of which are based on the condition of local thermal equilibrium. However, these spectroscopic techniques have only been demonstrated for relatively long time scales of $>10$ ns. The electron temperature can also be determined by measuring the expansion velocity of the shock wave generated by the plasma [33,34]. Measurements of plasmas produced by nanosecond pulses have been made in air using a cw probe in which the temporal resolution was limited by the gating of the CCD detection to the nanosecond time scale [33,34]. Subnanosecond electron temperature dynamics has largely remained unexplored.

We present measurements of the electron temperature and concentration dynamics in a femtosecond laser-induced plasma channel with picosecond temporal resolution in the noble gas series from He to Xe using four-wave mixing (FWM), following on our initial report [35]. The measurements are performed from the onset of plasma formation due to the 80-fs pump laser up to 1.5 ns [35] and provide a complement to the aforementioned methods yielding the early-time electron dynamics. In this work plasma formation is dominated by geometrical focusing, producing a single short plasma channel, and is not produced by self-focusing, thus avoiding multiple filamentation effects. A theoretical model based on electron impact ionization cooling is presented to predict electron kinetic energies evolving from $>20$ to $<1$ eV. We also demonstrate the use of the continuum fluorescence background resulting from Bremsstrahlung emission as a means to determine the relative concentrations of singly ionized atoms generated within the plasma. The essence of the ionization and subsequent cooling process is captured mainly by the ionization potential of the atom, affecting both tunnel ionization and impact ionization cooling. In this article, we provide a detailed description of the theoretical modeling along with further tests of the model by measuring the pressure and laser intensity effects on the electron dynamics in the plasma channel.

 

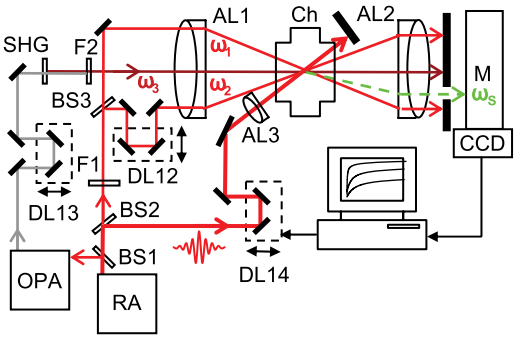


FIG. 1. (Color online) Experimental setup. RA—Ti:sapphire regenerative amplifier; OPA—optical parametric amplifier; BS1, BS2, BS3—beam splitters; DL12, DL13, DL14—retro-reflector-based optical delay lines; AL1, AL2, AL3—achromatic lenses; SHG—second harmonic generator; Ch—chamber; F1, F2—optical filters; M—monochromator; CCD—cooled CCD array detector.

## II. EXPERIMENT

The schematic of our experimental setup is shown in Fig. 1. Transform-limited pulses of 2.4 mJ centered at 800 nm were generated using a Ti:sapphire regenerative amplifier (RA) with a pulse duration of 80 fs and a repetition rate of 1 kHz. A beam splitter (BS1) was used to direct 1 mJ of the amplified beam to pump an optical parametrical amplifier (OPA). The remainder of the beam was further split 20:80 by the second beam splitter (BS2). The more intense portion was used as a pump beam for plasma generation. After passing through the computer-controllable delay line (DL14), this pump beam was focused by an achromatic lens (L3; 5 cm focal length) to generate the microplasma in a chamber (Ch) filled with the noble gas sample at a regulated pressure. The initial diameter (prior to the lens) of the pump beam was 2 mm. The remainder of the amplified beam, after BS2, was spectrally filtered to 1 nm full width half maximum (FWHM), corresponding to a 1-ps pulse duration, by a narrow-band optical filter (F1) and split 50:50 by a third beam splitter (BS3) to create two FWM beams of $\omega_1 = \omega_2 = 800$ nm. The third FWM beam (140 fs, 971 nm), $\omega_3$, was generated by doubling the fundamental of the idler from the OPA using a second-harmonic generator (SHG). The fundamental was cut off by a filter (F2). The $\omega_2$ and $\omega_3$ beams traverse optical delay lines (DL12 and DL13) to equalize the optical paths of all three FWM beams to achieve temporal overlap in the interaction region. All three FWM beams as well as the pump were polarized in the horizontal plane. An achromatic lens (AL1) was used to direct the three FWM beams into the optical chamber. The beam geometry was based on folded-BOXCARS [36] and provided complete angular separation of the emitted signal beam, $\omega_S$. The frequency of the $\omega_3$ beam and the angles at which the three FWM beams enter the focal point were chosen to fulfill the phase-matching conditions on the respective wavevectors, $\mathbf{k}_1 + \mathbf{k}_2 = \mathbf{k}_3 + \mathbf{k}_S$. For all the investigated gases, the OPA idler wavelength was set to generate the $\omega_S$ beam centered at 680 nm. The spectral region around 680 nm contains a minimal number of fluorescence peaks for all five gases investigated. The emitted FWM signal was collimated by an achromatic lens (AL2) and then passed through an iris to the monochromator (M) equipped with a cooled CCD array detector.

## III. RESULTS AND DISCUSSION

To probe the mechanism of laser-induced microplasma formation we first measured the fluorescence spectra of the plasma after excitation by the intense pump laser pulse ($\sim 10^{14}$ W cm$^{-2}$). The spectra are presented in Fig. 2(a) and each features an array of sharp peaks residing on a broad, flat background. The sharp features observed in each spectrum are related to electronic transitions in the corresponding neutral atom. The broad background is a continuum caused by the Bremsstrahlung emission [37]. The background for each of the various gases is well approximated by a horizontal straight line (dashed lines in Fig. 3) over the small spectral window measured here. The intensity of the Bremsstrahlung emission depends strongly on the number and energy of the free electrons, which in turn are determined by the gas ionization potential $I_p$ and the power of the plasma-generating beam. Indeed, doubling $I_p$ [from Xe (12.13 eV) to He (24.59 eV)] leads to a decrease in the background level of more than three orders of magnitude [Fig. 2(a)]. Increasing the pump laser power producing the plasma from 30 to 250 mW leads to an increase in the background signal of more than two orders of magnitude [Fig. 2(b)]. The measured background levels

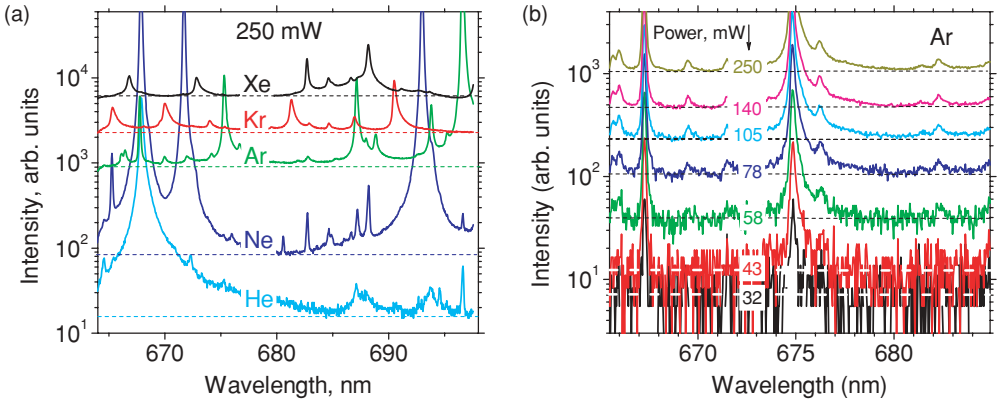


FIG. 2. (Color online) Fluorescence spectra of the plasma generated in different noble gases by the 250-mW pump laser pulse (a) and the same for Ar at different pump laser powers (b). Dashed lines represent the broad, flat background caused by Bremsstrahlung emission.

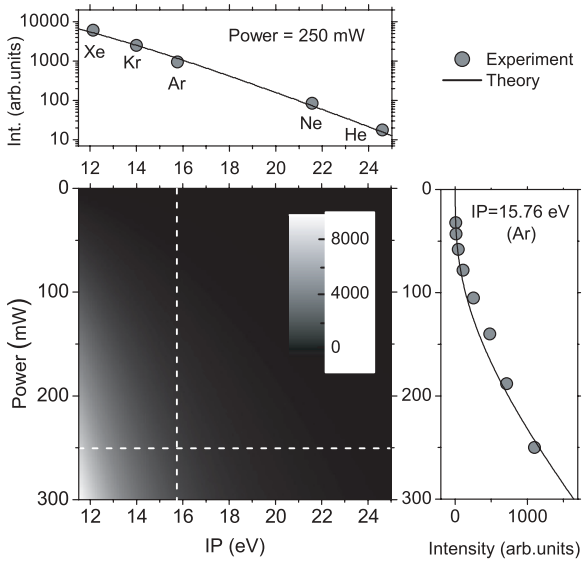


FIG. 3. Intensity of Bremsstrahlung background emission as a function of the pump beam power and the gas ionization potential, $I_P$, simulated according to ADK theory. The upper and right-side panels show the comparison of the theory with experiment. Upper panel: Intensity vs $I_P$ for a pump power of 250 mW (horizontal dashed line in the gray-scale map). Right panel: Intensity vs power for Ar, $I_P = 15.76$ eV (vertical dashed line). Experimental data are represented by gray circles; solid curves correspond to the simulation using Eq. (3).

are consistent with the tunnel character of the strong-field ionization of noble gas atoms and can be modeled using ADK theory [38] to calculate the ionization rate of an atom at any point in space and time as a function of the local electric field amplitude envelope, $E(\mathbf{r}, t)$.

Upon integration over the laser period and summation over the valence shell, the celebrated ADK formula [38] takes the form

$$W(\mathbf{r},t) = N\left(\frac{6}{\pi}\right)^{1/2}\frac{2^{2n^*}}{n^*\Gamma(2n^*)} \times\left(\frac{\mathcal{R}}{\hbar}\right)\left(\frac{I_p}{\mathcal{R}}\right)\left[\frac{4\mathcal{R}}{e|E(\mathbf{r},t)|a_B}\left(\frac{I_p}{\mathcal{R}}\right)^{3/2}\right]^{2n^*-3/2} \times\exp\left[-\frac{4\mathcal{R}}{3e|E(\mathbf{r},t)|a_B}\left(\frac{I_p}{\mathcal{R}}\right)^{3/2}\right], \quad (1)$$

where $N$ is the number of valence electrons and $n^* = (\mathcal{R}/I_p)^{1/2}$ is the effective principal quantum number, with $\mathcal{R}$ the Rydberg energy. To obtain the total degree of ionization in the interaction volume, we have to integrate Eq. (1) with the temporal and spatial profile of the electric field envelope. We assume that the pump laser pulse is transform-limited and that the transverse, cylindrically symmetric Gaussian profile is approximately constant over the entire length $l$ of the interaction volume. Then, the time-dependent local electric field envelope in the interaction volume is

$$E(\mathbf{r},t) = E_0\exp\left(-\frac{\rho^2}{2R^2}\right)\exp\left(-\frac{t^2}{\sigma}\right), \quad (2)$$

where $2(\sigma\ln 2)^{1/2}$ is the FWHM and $R$ is the beam waist radius. By following the approach used in Ref. [39] for multiphoton ionization by a square pulse, the total degree of ionization (the ratio of the number of ionized atoms to the total number of atoms in the interaction volume) is then obtained as

$$\eta = \int_0^{E_0}\frac{dE}{E}\left\{1-\exp\left[-\frac{12N(2\sigma)^{1/2}}{n^*\Gamma(2n^*)}\left(\frac{\mathcal{R}}{\hbar}\right)\left(\frac{8\mathcal{R}}{eE_0a_B}\right)^{2n^*-2} \times\left(\frac{I_p}{\mathcal{R}}\right)^{3n^*-2}\exp\left(-\frac{4\mathcal{R}}{3eE_0a_B}\left(\frac{I_p}{\mathcal{R}}\right)^{3/2}\right)\right]\right\} \quad (3)$$

and can be expressed as a fast-converging series of incomplete gamma functions [40],

$$\eta = \sum_{m=1}^{\infty}\frac{(-1)^{m+1}A^m}{m!}(m\beta)^{2m(1-n^*)}\Gamma\big(-2m(1-n^*), m\beta\big), \quad (4)$$

where

$$A = \frac{12N(2\sigma)^{1/2}}{(n^*)^{6n^*-3}\Gamma(2n^*)}\left(\frac{\mathcal{R}}{\hbar}\right)\left(\frac{8\mathcal{R}}{eE_0a_B}\right)^{2n^*-2}; \qquad \beta = \frac{4\mathcal{R}}{3eE_0a_B(n^*)^3}. \quad (5)$$

Equations (4) and (5) predict an exponentially strong dependence of the total degree of ionization on both the laser field amplitude, $E_0$, and the ionization potential as expressed by the effective quantum number, $n^*$.

Figure 3 shows the simulation of the Bremsstrahlung background emission intensity as a function of both the power of the pump beam and $I_P$ of the gas using Eq. (4) in comparison with experimental measurements. In the simulation we assumed that the Bremsstrahlung emission intensity is proportional to the total degree of ionization, $\eta$, because the signal is integrated over 1 ms. Experimental values of the intensity of the Bremsstrahlung emission (circles) in the upper panel (emission intensity versus $I_P$) were extracted directly from the spectra shown in Fig. 2(a). The right panel (emission intensity versus laser power) shows the experimental points extracted from the spectra presented in Fig. 2(b). The solid curves in both panels were simulated using Eq. (4) at a constant value of the laser power, 250 mW (upper panel), and a constant ionization potential of 15.76 eV (right panel). The agreement between theory and experiment suggests that the ionization is indeed dominated by the tunnel mechanism and that the model is capable of predicting quantitatively the ionization probability in atmospheric-pressure noble gas plasmas induced by strong-field laser pulses, as a function of the laser power and the noble gas ionization potential.

To calculate the electron dynamics after ionization we consider that once the free electrons emerge from the tunnel ionization, they immediately accelerate to higher kinetic energies by ponderomotive action of the strong laser field. This ponderomotive energy of an individual electron would return to zero after the laser pulse decreased to zero intensity [41,42]. However, these laser-field-driven electrons can (and do) effectively scatter from one another and from the ions, thus nonadiabatically transforming the ponderomotive energy into the energy of the emerging plasma provided the pressure

is high enough. As inelastic scattering continues after the pulse is over, the electron temperature is established on a subpicosecond time scale. Then, we can assume that the electrons are characterized by a thermal distribution function at any step during the subsequent, and slower, process of plasma cooling. As an approximation, we assume that the energy loss is mainly due to impact ionization of the remaining neutral atoms. (By assuming so, we neglect the possibility of multiple ionization as well as impact excitation of atoms and ions to higher lying bound electronic states.) Then, the energy balance in the acts of ionization can be expressed as

$$\frac{d}{dt}\left(\frac{3}{2}nT\right) + I_p\frac{dn}{dt} = 0, \tag{6}$$

where $I_p$ is the ionization potential, $T$ is the electron temperature, and $n$ is the electron concentration, whose evolution, in turn, is determined by the rate equation,

$$\frac{dn}{dt} = \nu(t)n(n_0 - n), \tag{7}$$

with $\nu(t)$ representing the temperature-dependent ionization rate and $n_0$ representing the initial concentration of neutral atoms. Equations (6) and (7) constitute a system of coupled differential equations for the concerted evolution of $T$ and $n$. A pivotal role in the cooling process is played by the ionization rate given by the ensemble average of the product of energy-dependent ionization cross secion, $\sigma(E)$, and the electron velocity value, $v$: $\nu(t) = \langle\sigma v\rangle$. Assuming Maxwellian distribution for the thermalized electrons, we have

$$\nu(T) = 2\sqrt{\frac{2\pi}{mT^3}}\int_{I_p}^{\infty} dE\, E\sigma(E)\exp\left(-\frac{E}{T}\right). \tag{8}$$

As seen from Eq. (8), the high-energy tail of the electron distribution is responsible for creating additional ions from neutrals, because only sufficiently energetic free electrons (with kinetic energy $E > I_p$) are capable of ionizing bound electrons in the remaining neutral atoms. When these energetic electrons collide with atoms to create ions, the high-energy tail tends to be depleted, only to be replenished by the ascendance of lower energy electrons via thermal equilibration. This process goes on at the cost of lowering the electron temperature, much like the evaporation cooling to produce ultracold gases [43–45]. Thus, the continuing process of impact ionization both increases the number of free electrons and further cools their distribution.

To calculate the cooling rate we require the cross section for ionization to be a function of electron kinetic energy. Although there is ongoing discussion in the literature as to which semi-empirical expression for $\sigma(E)$ would be the best at intermediate values of energy $E - I_p \sim I_p$ with which we are concerned, the general agreement is that the cross section scales with the ionization potential and the number of electrons in the upper shell, $N$, as

$$\sigma(E) = N\left(\frac{\mathcal{R}}{I_p}\right)^2 \pi a_B^2\tilde{\sigma}(u), \tag{9}$$

where $a_B$ is the Bohr radius and $u = (E/I_p) - 1$. The reduced ionization cross section of a given atomic species as a function of electron kinetic energy is represented in Eq. (9) by a dimensionless function, $\tilde{\sigma}(u)$, which will be defined subsequently for the energy regime under investigation. Using Eq. (9) in Eq. (8) leads to a universal expression for the ionization rate as a function of dimensionless temperature, $\theta = T/I_p$:

$$\nu(\theta) = t_0 a_B^3\tilde{\nu}(\theta); \tag{10}$$

$$t_0 = 2\sqrt{\pi}\frac{\mathcal{R}}{\hbar}N\left(\frac{\mathcal{R}}{I_p}\right)^{\frac{3}{2}},$$
$$\tilde{\nu}(\theta) = \theta^{-\frac{3}{2}}e^{-\frac{1}{\theta}}\int_0^{\infty} du\,\tilde{\sigma}(u)(u+1)e^{-\frac{u}{\theta}}. \tag{11}$$

The plasma evolution can then be described by the coupled dimensionless equations for $\theta$ and the degree of ionization, $\eta$, the ratio of the number of ionized atoms to the total number of atoms, as functions of dimensionless time,

$$\tau = \frac{t}{t_0 n_0 a_B^3}. \tag{12}$$

These equations read

$$\frac{d\theta}{d\tau} = -\left(\theta + \frac{2}{3}\right)\tilde{\nu}(\theta)\,(1-\eta),$$
$$\frac{d\eta}{d\tau} = \tilde{\nu}(\theta)\,\eta\,(1-\eta). \tag{13}$$

From these equations, the degree of ionization is expressed in terms of the dimensionless temperature $\theta$ as

$$\eta = \eta(0)\frac{\theta(0) + 2/3}{\theta + 2/3}, \tag{14}$$

where $\theta$, in turn, is determined by the equation

$$\frac{d\theta}{d\tau} = -\tilde{\nu}(\theta)(\theta - \theta_f),$$
$$\theta_f = \left[\eta(0)\left(\theta\,(0) + \frac{2}{3}\right) - \frac{2}{3}\right]. \tag{15}$$

At this stage, we finally need to specify $\tilde{\nu}(\theta)$ by identifying the expression for the reduced ionization cross section $\tilde{\sigma}(u)$. We use a simple semiempirical approximation known as the Lotz formula [46],

$$\tilde{\sigma}(u) = \gamma\frac{\ln(u+1)}{u+1}, \tag{16}$$

where $\gamma$ is a fitting parameter. This approximation results in the functional dependence $\tilde{\nu}(\theta) = -(\gamma/\sqrt{\theta})\mathrm{Ei}(-1/\theta)$, where $\mathrm{Ei}(z)$ is the integral exponential function [39]. By using this expression for $\tilde{\nu}(\theta)$ in Eq. (15), $\theta(\tau)$ is obtained implicitly in a quadrature form,

$$\int_{\theta(0)}^{\theta}\frac{\sqrt{\theta'}d\theta'}{\mathrm{Ei}\left(-\frac{1}{\theta'}\right)(\theta' - \theta_f)} = \gamma\tau. \tag{17}$$

The evolution of the dimensionless degree of ionization, $\eta(\tau)$, and dimensionless temperature, $\theta(\tau)$, is determined by Eqs. (14) and (17). Ultimately, this evolution depends on the initial values, $\eta(0)$ as found from Eq. (4), and on $\theta(0) \sim 1$. The dimensionalized functions $n(t)$ and $T(t)$, in turn, determine the response of the plasma to external fields, and, in particular, the intensity of the four-wave-mixing scattering.

To measure the temperature of the electrons as a function of time, we employ an ultrafast four-wave mixing method where a dynamic grating is imposed on the plasma by the probe laser beams and the degree of scattering is measured as a function of time after initiating the microplasma. There are two major mechanisms contributing to the FWM signal intensity in a plasma: 1. the electron density grating due to the ponderomotive potential of the $\omega_1$, $\omega_2$, and $\omega_3$ beams and 2. the electron temperature grating due to local heating. For the femtosecond pulses used in our experiments, only the first mechanism is relevant, and that is well described in the framework of hydrodynamic plasma equations. Following Ref. [47], one has that the density grating imposed by two electromagnetic waves with amplitudes $A_1$ and $A_2$, directional unit vectors $\mathbf{n}_1$ and $\mathbf{n}_2$, and spectral functions $f_1(\omega)$ and $f_2(\omega)$, respectively, is given by

$$\tilde{n}(\omega,\mathbf{k}) = \frac{A_1 A_2}{32\pi mc^2}\frac{\omega_p^2 k^2}{\left(\omega^2-\omega_p^2-\frac{\gamma T}{m}k^2\right)} \times \int d\omega' \mathbf{(}f_1(\omega')f_2(\omega'-\omega)+f_1(-\omega')f_2(\omega-\omega')\mathbf{)} \times \delta\mathbf{(}\mathbf{k}-\mathbf{n}_1 k(\omega')+\mathbf{n}_2 k(\omega'-\omega)\mathbf{)}, \quad (18)$$

where $\omega_p$ is the plasma frequency. In the setup depicted in Fig. 1, the two waves of Eq. (18) are the beams $\omega_1$ and $\omega_3$. As the spectral width of these beams is much smaller than $\omega_p$,

$$\tilde{n}(\omega,\mathbf{k}) \propto \frac{\omega_p^2 k^2}{\left[(\omega_1-\omega_3)^2-\omega_p^2-\frac{\gamma T}{m}k^2\right]} \propto \frac{n(t)}{T(t)}. \quad (19)$$

Thus, the dependence of the measured intensity of the scattered light on the plasma parameters may be approximated as

$$I \propto [n(0)]^2 \frac{\left[\theta(0)+\frac{2}{3}\right]^2}{\theta^2\left(\theta+\frac{2}{3}\right)^2}. \quad (20)$$

The evolution of the electronic temperature $T$ for the noble gases was determined as a function of time according to simulation using Eq. (17). The trend, demonstrated in Fig. 4(a), shows that the cooling rate increases from He to Xe. An order of magnitude decrease in the electron temperature of Xe plasma is observed within the first 250 ps after the plasma formation. Tracking such rapid dynamics was made possible in our measurements because the temporal resolution is increased by several orders of magnitude compared to the previous nanosecond measurements [29,30,33,34]. The higher cooling rate of the noble gases with lower values of $I_p$ is manifest in the intensity evolution of the FWM signal generated in the microplasma. The experimental measurement of the FWM signal generated versus $\tau_{14}$ delay (circles) is shown in Fig. 4. These measurements were performed in the spectral region from 676 to 686 nm [shadowed region in the inset to Fig. 4(b)] where there is a minimum in the number of fluorescence lines for all of the gases investigated. A typical spectrum of the FWM signal is represented by the black curve shown in the inset for Kr at 250 mW ($\tau_{14}$ = 1000 ps). The spectrum has a Gaussian-like shape, defined by the spectral phase mismatch for fs-BOXCARS [48]. The time-dependent measurements display a rise time that is dictated by the impact ionization cooling rate. The increasing rate of plasma cooling from He to Xe corresponds directly to the rate at which the FWM signal increases. As the electrons cool, the ponderomotive grating formed by beams $\omega_1$ and $\omega_3$ is established with higher contrast between the regions of constructive and destructive interference, thus increasing the magnitude of the FWM signal. After ~250 ps the Xe FWM signal begins to reach a plateau in accordance with the results obtained in Fig. 4(a) where the rate of change for the electron temperature is seen to dramatically taper off. The magnitude of the FWM signal directly reflects the degree of ionization within the microplasma. As expected from Fig. 2(a), the noble gas species with the lowest IP will generate the greatest abundance of electrons. Hence, the magnitude of the FWM signal increases from He to Xe in the plateau region. The calculated FWM scattering intensity using Eq. (20) is shown for the noble gases investigated as the solid curves in Fig. 4(b). As seen from Eq. (20), each gas has a time dependence for the FWM signal intensity $I$ that is governed by the time dependence of the dimensionless electronic temperature $\theta = T/I_p$. The theoretical predictions

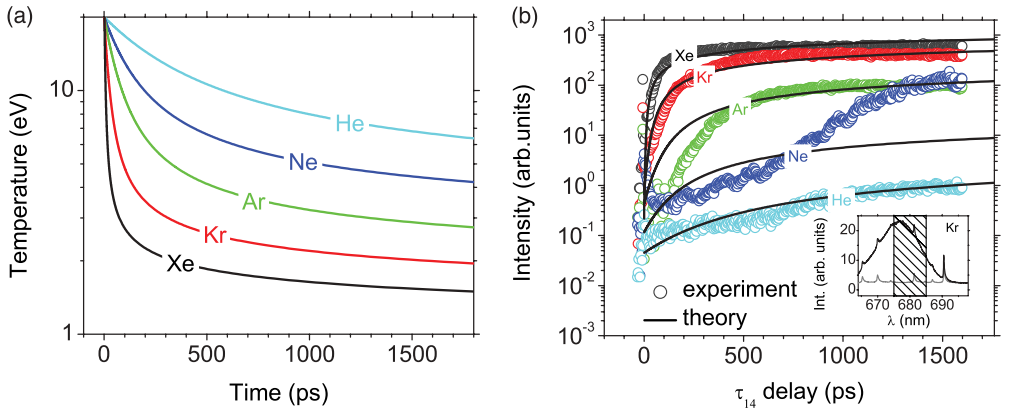


FIG. 4. (Color online) (a) Time dependence of the electron temperature $T$ for the series of noble gases as calculated with the ionization cooling model. (b) The intensity of the FWM signal for the five noble gases plotted vs $\tau_{14}$ delay, measured at the spectral position near the maximum of the FWM signal (circles). The FWM signal intensity vs time as simulated by our theoretical model (solid lines) is also shown. The inset shows the FWM (black curve) and fluorescence (gray curve) spectra of Kr. The spectral region where the time-resolved signal was accumulated is shadowed.

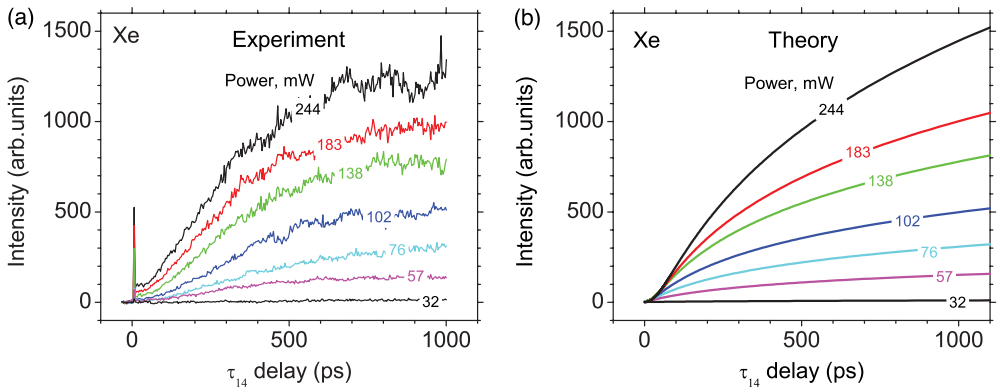


FIG. 5. (Color online) Intensity of the FWM signal for Xe vs $\tau_{14}$ delay, measured at the spectral position near the maximum of the FWM signal for different values of the pump beam power: (a) experiment; (b) theory.

agree with the experimental data quite well, with the exception of Ne.

This Ne exception is especially notable given the fact that Ne follows the trend with respect to the total degree of ionization, as expressed in Fig. 3, suggesting that the underlying plasma evolution should not be different from the other noble gases. The considerable increase of the signal for Ne after 500 ps is presumably due to the very strong emission lines in close vicinity of the FWM signal detection window from 676 to 686 nm, as seen in Fig. 2(a). These Ne emission lines dwarf all other emission lines observed, including those for the remaining noble gases. The Ne lines, at 667.8, 671.7, and 692.9 nm, are immediately adjacent to the observation window and the broad tails of these lines extend well into the detection region and can affect the propagating FWM signal. As the plasma cooling evolution proceeds, the excited states corresponding to these transition lines become populated, leading to population inversion [49]. Then, the FWM signal induces stimulated emission from the excited state population in the observation window, resulting in significant amplification. This scenario agrees well with the fact that the deviant Ne behavior emerges later in the process of the cooling evolution. We note that the Bremsstrahlung data shown Fig. 2(a) are accumulated over a period of about 1 ms. On the much shorter time scales of the FWM measurements probing the microplasma evolution [<1 ns, as shown in Fig. 4(b)], the emission line broadening will be much more pronounced, resulting in even more significant tailing into the detection window, further exacerbating the impact.

We can further test the model by investigating the microplasma response as a function of pump laser power and gas pressure. Increasing the power of the laser inducing the microplasma should alter the electron cooling dynamics because higher intensities will cause both a higher density and a higher initial temperature of the electrons produced. Thus, investigations of the dynamics as a function of laser power will test the predictive ability of the theoretical model. The measurements of the FWM scattering intensity as a function of delay after the microplasma is generated are shown in Fig. 5(a) for Xe at laser powers ranging from 32 to 244 mW. The sharp increase in the magnitude of the FWM signal with laser power reflects the increase in electron concentration due to the higher probability for laser-induced tunnel ionization. This is in agreement with the measurement of the Bremsstrahlung emission as a function of laser power that is presented in Fig. 2(b). The rise time of the FWM signal also depends upon the laser power. The trend of decreasing rise time with increasing laser intensity is a direct reflection of the electron temperature dynamics. Hotter electrons, produced at higher laser powers, cool more rapidly due to the increased cross section for impact ionization. The results of the corresponding simulation using Eq. (20) are shown in Fig. 5(b). For each given value of the pump laser power, the key parameters that determine the simulated plasma cooling evolution, $n(0)$ and $\theta(0)$, were extracted from the simulation for the data shown in Fig. 3. The agreement between the theoretical predictions and the experimental measurements suggests that the theory is able to predict both the temporal and laser-power dependence of the FWM signal intensity for a laser-induced microplasma.

The dependence of the FWM signal on the target gas pressure can be gleaned from the expression for the dimensionless time variable of Eq. (12), $\tau = t/(t_0 n_0 a_B^3)$. This expression reveals that the characteristic cooling time of the plasma dynamics scales proportionally to the inverse of the gas pressure $P$, as reflected in the initial number density of neutral atoms, $n_0 \sim P$. We have introduced a parameter $\tau_{1/2}$ that corresponds to the ramp time required for the FWM signal to reach half of its plateau intensity (see inset in Fig. 6). According to Eq. (12), the parameter $\tau_{1/2}$ should be inversely proportional to $P$. Figure 6 represents the parameter $\tau_{1/2}$

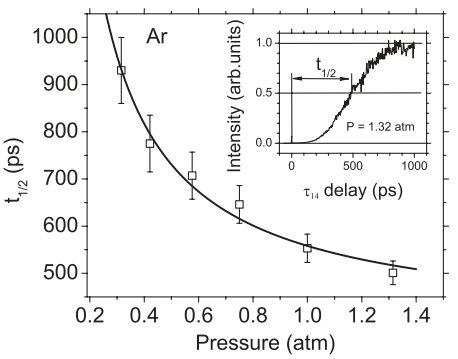


FIG. 6. (a) Parameter $t_{1/2}$ as a function of gas pressure in Ar. The inset shows a typical normalized intensity time dependence for pressure $P = 1.32$ atm.

extracted from measurements for Ar at 250 mW versus the gas pressure $P$ and the fit with a simple hyperbolic function $\tau_{1/2} = A/P$, where $A$ is a fitting parameter. In accordance with the theoretical model, the experimental measurements indicate that the $\tau_{1/2}$ parameter does in fact scale hyperbolically with pressure in the entire interval from ~0.3 to 1.32 atm. The time required to cool the plasma is reduced at higher gas pressures because there is a greater initial concentration of neutral species, $n_0$, available to ionize and remove the high kinetic energy portion of the electron distribution. According to Eq. (7), increasing $n_0$ increases the probability for electron-neutral collisions, thus allowing for more rapid cooling via impact ionization. The eventual magnitude of the FWM signal has also been observed to increase with pressure (data not shown), apparently due to the greater abundance of electrons available to participate in the FWM.

## IV. CONCLUSIONS

We have presented a theoretical model for the electron concentration and kinetic energy distribution dynamics for a microplasma induced by an 80-fs laser pulse. The model is based on initial tunnel ionization followed by electron impact ionization cooling. The model reproduces well the measured degree of ionization in an atmospheric-pressure laser-induced plasma. The model predicts the intensity of four-wave mixing as a function of time for a series of five noble gases, He, Ne, Ar, Kr, and Xe, revealing that the measured intensity is primarily a function of electron cooling dynamics. The model also predicts the dynamics as a function of pump laser intensity and gas pressure. The findings open the way for effective control of microplasma dynamics.


[1] A. L'Huillier and P. Balcou, Phys. Rev. Lett. **70**, 774 (1993).

[2] J. J. Macklin, J. D. Kmetec, and C. L. Gordon III, Phys. Rev. Lett. **70**, 766 (1993).

[3] N. A. Papadogiannis, B. Witzel, C. Kalpouzos, and D. Charalambidis, Phys. Rev. Lett. **83**, 4289 (1999).

[4] M. Hentschel, R. Kienberger, Ch. Spielmann, G. A. Reider, N. Milosevic, T. Brabec, P. Corkum, U. Heinzmann, M. Drescher, and F. Krausz, Nature (London) **414**, 509 (2001).

[5] P. M. Paul, E. S. Toma, P. Breger, G. Mullot, F. Auge, Ph. Balcou, H. G. Muller, and P. Agostini, Science **292**, 1689 (2001).

[6] S. Tzortzakis, G. Mechain, G. Patalano, Y.-B. Andre, B. Prade, M. Franco, A. Mysyrowicz, J.-M. Munier, M. Gheudin, G. Beaudin, and P. Encrenaz, Opt. Lett. **27**, 1944 (2002).

[7] K. Y. Kim, J. H. Glownia, A. J. Taylor, and G. Rodriguez, Opt. Express **15**, 4577 (2007).

[8] C. D. Amico, A. Houard, S. Akturk, Y. Liu, J. Le Bloas, M. Franco, B. Prade, A. Couairon, V. T. Tikhonchuk, and A. Mysyrowicz, New J. Phys. **10**, 013015 (2008).

[9] A. Braun, G. Korn, X. Liu, D. Du, J. Squier, and G. Mourou, Opt. Lett. **20**, 73 (1995).

[10] M. Rodriguez, R. Bourayou, G. Mejean, J. Kasparian, J. Yu, E. Salmon, A. Scholz, B. Stecklum, J. Eisloffel, U. Laux, A. P. Hatzes, R. Sauerbrey, L. Woste, and J.-P. Wolf, Phys. Rev. E **69**, 036607 (2004).

[11] N. Akozbek, M. Scalora, C. M. Bowden, and S. L. Chin, Opt. Commun. **191**, 353 (2001).

[12] P. B. Corkum, Phys. Rev. Lett. **71**, 1994 (1993).

[13] C. Y. Chien, B. La Fontaine, A. Desparois, Z. Jiang, T. W. Johnston, J. C. Kieffer, H. Pepin, F. Vidal, and H. P. Mercure, Opt. Lett. **25**, 578 (2000).

[14] H. Yang, J. Zhang, Y. J. Li, J. Zhang, Y. T. Li, Z. L. Chen, H. Teng, Z. Y. Wei, and Z. M. Sheng, Phys. Rev. E **66**, 016406 (2002).

[15] J. S. Liu, Z. L. Duan, Z. N. Zeng, X. H. Xie, Y. P. Deng, R. X. Li, Z. Z. Xu, and S. L. Chin, Phys. Rev. E **72**, 026412 (2005).

[16] M. Centurion, Y. Pu, Z. W. Liu, D. Psaltis, and T. W. Hansch, Opt. Lett. **29**, 772 (2004).

[17] M. Centurion, Y. Pu, and D. Psaltis, J. Appl. Phys. **100**, 063104 (2006).

[18] G. Rodriguez, A. R. Valenzuela, B. Yellampalle, M. J. Schmitt, and K. Y. Kim, J. Opt. Soc. Am. B **25**, 1988 (2008).

[19] S. Tzortzakis, B. Prade, M. Franco, and A. Mysyrowicz, Opt. Commun. **181**, 123 (2000).

[20] R. P. Fischer, A. C. Ting, D. F. Gordon, R. F. Ferrisler, G. P. DiComo, and P. Sprangle, IEEE Trans. Plasma Sci. **35**, 1430 (2007).

[21] X. L. Mao, S. S. Mao, and R. E. Russo, Appl. Phys. Lett. **82**, 697 (2003).

[22] S. Minardi, A. Gopal, M. Tatarakis, A. Couairon, G. Tamosauskas, R. Piskarskas, A. Dubietis, and P. Di Trapani, Opt. Lett. **33**, 86 (2008).

[23] Q. Sun, H. B. Jiang, Y. Liu, Z. X. Wu, H. Yang, and Q. H. Gong, Opt. Lett. **30**, 320 (2005).

[24] A. Gopal, S. Minardi, and M. Tatarakis, Opt. Lett. **32**, 1238 (2007).

[25] F. Theberge, W. W. Liu, P. T. Simard, A. Becker, and S. L. Chin, Phys. Rev. E **74**, 036406 (2006).

[26] S. A. Hosseini, Q. Luo, B. Ferland, W. Liu, S. L. Chin, O. G. Kosareva, N. A. Panov, N. Akozbek, and V. P. Kandidov, Phys. Rev. A **70**, 033802 (2004).

[27] H. R. Griem, *Spectral Line Broadening by Plasmas* (Academic Press, New York, 1974).

[28] G. Bekefi, *Principles of Laser Plasmas* (Wiley Interscience, New York, 1976).

[29] B. Le Drogoff, J. Margot, M. Chaker, M. Sabsabi, O. Barthelemy, T. W. Johnston, S. Laville, F. Vidal, and Y. von Kaenel, Spectrochim. Acta B **56**, 987 (2001).

[30] X. Zeng, X. L. Mao, R. Greif, and R. E. Russo, Appl. Phys. A **80**, 237 (2005).

[31] G. J. Bastiaans and R. A. Mangold, Spectrochim. Acta B **40**, 885 (1985).

[32] H. R. Griem, *Principles of Plasma Spectroscopy* (Cambridge University Press, Cambridge, 1997).

[33] M. Villagran-Muniz, H. Sobral, and E. Camps, IEEE Trans. Plasma Sci. **29**, 613 (2001).

[34] M. Thiyagarajan and J. Scharer, J. Appl. Phys. **104**, 013303 (2008).
[35] A. Filin, R. Compton, D. A. Romanov, and R. J. Levis, Phys. Rev. Lett. **102**, 155004 (2009).
[36] A. C. Eckbreth, Appl. Phys. Lett. **32**, 421 (1978).
[37] T. Fujimoto, *Plasma Spectroscopy* (Oxford University Press, New York, 2004).
[38] M. V. Ammosov, N. B. Delone, and V. P. Krainov, Sov. Phys. JETP **64**, 1191 (1986).
[39] S. M. Hankin, D. M. Villeneuve, P. B. Corkum, and D. M. Rayner, Phys. Rev. A **64**, 013405 (2001).
[40] M. Abramowitz and I. A. Stegun, eds., *Handbook of Mathematical Functions With Formulas, Graphs, and Mathematical Tables*, NBS Applied Mathematics Series 55 (National Bureau of Standards, Washington, DC, 1964).
[41] T. W. B. Kibble, Phys. Rev. **150**, 1060 (1966).
[42] P. H. Bucksbaum, R. R. Freeman, M. Bashkansky, and T. J. Mcllrath, J. Opt. Soc. Am. B **4**, 760 (1987).
[43] C. E. Wieman, D. E. Pritchard, and D. J. Wineland, Rev. Mod. Phys. **71**, S253 (1999).
[44] J. D. Weinstein, R. deCarvalho, C. I. Hancox, and J. M. Doyle, Phys. Rev. A **65**, 021604(R) (2002).
[45] C. I. Hancox, S. C. Doret, M. T. Hummon, L. J. Luo, and J. M. Doyle, Nature (London) **431**, 281 (2004).
[46] S. M. Younger and T. D. Mark, in *Electron Impact Ionization*, edited by T. D. Mark and G. H. Dunn (Springer-Verlag, Vienna, New York, 1985), p. 24.
[47] D. G. Steel and J. F. Lam, Opt. Lett. **4**, 363 (1979).
[48] D. Romanov, A. Filin, R. Compton, and R. Levis, Opt. Lett. **32**, 3161 (2007).
[49] R. Compton, A. Filin, D. A. Romanov, and R. J. Levis, Phys. Rev. Lett. **103**, 205001 (2009).